

The prototype colliding-wind pinwheel WR 104

Peter G. Tuthill

School of Physics, University of Sydney, NSW 2006, Australia

p.tuthill@physics.usyd.edu.au

John D. Monnier

University of Michigan at Ann Arbor, Department of Astronomy, 500 Church Street, Ann Arbor, MI 48109-1090, USA

monnier@umich.edu

Nicholas Lawrance

School of Aerospace, Mechanical and Mechatronic Engineering, University of Sydney, NSW 2006, Australia

n.lawrance@acfr.usyd.edu.au

William C. Danchi

NASA Goddard Space Flight Center, Infrared Astrophysics, Code 685, Greenbelt, MD 20771, USA

wcd@iri1.gsfc.nasa.gov

Stan P. Owocki

Bartol Research Institute, University of Delaware, Newark, DE 19716

owocki@bartol.udel.edu

and

Kenneth G. Gayley

University of Iowa, Iowa City, IA 52245

ken.gayley@gmail.com

ABSTRACT

Results from the most extensive study of the time-evolving dust structure around the prototype “Pinwheel” nebula WR 104 are presented. Encompassing 11 epochs in three near-infrared filter bandpasses, a homogeneous imaging data set spanning more than 6 years (or 10 orbits) is presented. Data were obtained from the highly successful Keck Aperture Masking Experiment, which can recover high fidelity images at extremely high angular resolutions, revealing the geometry of the plume with unprecedented precision. Inferred properties for the (unresolved) underlying binary and wind system are orbital period 241.5 ± 0.5 days and angular outflow velocity of 0.28 ± 0.02 mas/day. An optically thin cavity of angular size 13.3 ± 1.4 mas was found to lie between the central binary and the onset of the spiral dust plume. Rotational motion of the wind system induced by the binary orbit is found to have important ramifications: entanglement of the winds results in strong shock activity far downstream from the nose of the bowshock. The far greater fraction of the winds participating in the collision may play a key role in gas compression and the nucleation of dust at large radii from the central binary and shock stagnation point. Investigation of the effects of radiative braking pointed towards significant modifications of the simple hydrostatic colliding wind geometry, extending the relevance of this phenomena to wider binary systems than previously considered. Limits placed on the maximum allowed orbital eccentricity of $e \lesssim 0.06$ argue strongly for a prehistory of tidal circularization in this system. Finally we discuss the implications of Earth’s polar ($i \lesssim 16^\circ$) vantage point onto a system likely to host supernova explosions at future epochs.

Subject headings: stars: individual(WR 104), stars: mass loss, instrumentation: interferometers, stars: imaging, stars:winds, outflows

1. Introduction

The first well-resolved images of the dusty, IR-luminous Wolf-Rayet star WR 104 revealed an elegant plume stretching hundreds of AU from the bright core and following a trajectory closely matched to an Archimedean spiral (Tuthill et al. 1999). The origin of this geometry is simple and highly intuitive: material is embedded within a uniformly-expanding spherical wind driven from the hot stars at the heart of the system, yet the orbital motion of a central binary causes a rotating wake embedded within the flow. These images gave immediate confirmation of the colliding-wind binary nature of dust production in WR 104, and at the same time presented astronomy with a new type of object for study: a “Pinwheel”

nebula.

Although we found no specific predictions in the literature for such a spiral dust plume in dusty Wolf-Rayets such as WR 104, the same combination of orbital and outflow motions led Kuiper (1941) to predict exactly this geometry for the circumstellar environment around the eclipsing binary β Lyr. In fact use of the term “Pinwheel” to describe such a structure can be found as early as 1950 (Struve 1950), and theoretical study of colliding-wind binary systems has since developed an extensive literature (e.g. Stevens et al. 1992; Walder & Folini 2000, and refs therein). The basic picture of colliding-winds mediating dust production was formulated to explain the episodic dust-producer WR 140, which became something of a ‘Rosetta Stone’ system in important papers establishing the model (Williams et al. 1990; Usov 1991). It is also interesting, although perhaps tangential to the work of this paper, to note that Archimedian spirals may arise in quite distinct mass-loss environments such as the binary reflex-motion induced structure recently seen in AFGL 3068 (Mauron & Huggins 2006).

Observational confirmation of the pinwheel nebula around WR 104 has not yet been attained by adaptive optics imaging due to the requirement for a stable, well characterized point-spread function enabling recovery of structure at the diffraction limit (Rajagopal et al. 2004). However, a number of other techniques have been used to confirm the presence of the spiral plume including high spatial resolution lunar occultations (Mondal & Chandrasekhar 2002), variations in the visible lightcurve of 241 days in accord with the orbital period derived from interferometry (Kato et al. 2002), together with extensive follow-on observations with aperture masking interferometry (Tuthill et al. 2002, 2003; Monnier et al. 2007). Reports of binarity in the WR 104 system (Crowther 1997) appeared shortly before the original discovery of the spiral, with the spectral classification for the object given in van der Hucht (2001) as WC9d + B0.5V (+VB), although given the uncertainties we refer to the second component spectrum (actually brighter by a factor of ~ 2) as OB. Detailed radiative transfer modelling, confirming the appearance and basic observational properties of the pinwheel, has been performed by Harries et al. (2004).

The discovery of similar structures in an expanding list of host systems has served to motivate further interest in these objects. The second such system to be found, WR 98a (Monnier et al. 1999), showed a similar morphology implying approximately matched basic properties (in terms of orbital period and windspeed) to the prototype WR 104. However, a more diverse population is also coming to light including WR 112 (Marchenko et al. 2002) which appears to have a significantly longer 25 yr binary period, and the high orbital eccentricity 8 yr system WR 140 whose periodic periastron passages have been shown to throw off a remarkable series of dusty arcs (Monnier et al. 2002; Marchenko & Moffat 2006). Recently,

a dramatic association of at least two and probably five such spiral systems was discovered near the Galactic Center at the heart of the massive Quintuplet Cluster (Tuthill et al. 2006).

The status of Wolf-Rayets as candidate progenitors to type Ib/c supernovae (reviews can be found in Bethe 1990; Vanbeveren et al. 1998; Woosley et al. 2002) has generated considerable interest in their mass loss histories. In particular, structures within the circumstellar environment, into which the supernova blast wave expands, have the capacity to interact with the ejecta modifying the lightcurve and observed properties of the explosion. Indeed, Ryder et al. (2004) observed a residual fluctuating or rippled signal, obtained when subtracting a spherical best-fit model from the observed radio lightcurve of supernova 2001ig. The most likely interpretation for these modulations, they argue, arises as the supernova shock encounters periodic density enhancements embedded in the circumstellar environment by a colliding-wind binary pinwheel system. With the rapidly solidifying links between supernovae and gamma-ray bursts (Woosley & Bloom 2006), the mechanisms by which such mass-loss signatures may become encoded within the lightcurves of the most energetic explosions in the cosmos are being explored (Moran & Reichart 2005).

In this paper, we present the results of the most extensive diffraction-limited imaging study yet performed on the prototype pinwheel system, WR 104. Observations encompass three different near-infrared filter bandpasses and eleven distinct epochs covering more than six years (almost ten orbital periods) of the system. With the structure of the time-evolving plume revealed in unprecedented detail, we are able to address key outstanding questions regarding the way in which the dust formation is mediated by the colliding winds of the binary. Multi-wavelength observations are helpful in teasing apart the complex three-dimensional geometrical, thermal and illumination effects which go into creating the phenomena we see as a pinwheel nebula.

2. Observations

Monitoring of a number of dust-forming Wolf-Rayet stars was performed as part of our aperture-masking interferometry program begun at the Keck 1 telescope in 1996. This has produced astrophysical results spanning a range of different areas within contemporary stellar physics including studies of young stars (Danchi et al. 2001; Tuthill et al. 2002); evolved pulsating stars and giants (Tuthill et al. 2000; Monnier et al. 2004); and dusty mass-loss shrouds in proto-planetary nebulae and transition objects (Monnier et al. 2000; Tuthill et al. 2002). A full description of the experiment including a discussion of the conceptual principles and signal-to-noise considerations underlying masking interferometry is given in Tuthill et al. (2000) while further discussion of systematics and seeing induced errors can be found in

Monnier et al. (2004).

Observations presented here all used a partially-redundant annular mask geometry first suggested by Haniff & Buscher (1992) which was found to deliver robust imaging for targets as faint as $m_K \sim 6$ mag with complete Fourier coverage out to the 8 m maximum baseline passed by the mask. The detector used for this work was the NIRC camera with image magnifying front-optics modifying the plate scale so as to sample the diffraction-limited beam (Matthews et al. 1996). A relatively rapid-exposure ($T_{int} = 0.14$ sec) and high data volume (data cubes containing 100 frames) speckle observing mode was utilized, although this was not as well developed as it could have been and suffered from an inherent low duty cycle of at best 20% set by the camera electronics.

Observations of science targets were interleaved with those of nearby unresolved point-spread function (PSF) reference stars, and the extraction of calibrated visibility and closure-phase data followed established practices within speckle or masking interferometry (Tuthill et al. 2000). All V^2 and closure phase data products were stored in the FITS-based Optical Interferometry data exchange format (OI-FITS Pauls et al. 2005), and are available on request from the authors. Images were recovered using a number of different numerical methods including the CLEAN algorithm (Högbom 1974) and with several maximum entropy (Gull & Skilling 1984) based methods (Sivia 1987; Ireland et al. 2006). With some variation in levels of fidelity and resolution obtained, all methods produced similar structures to those presented in the following sections, and hereafter we show exclusively the results of the VLBMEM package (Sivia 1987).

A journal of masking observations of WR 104 is given in Table 1, while information about the three interference filters within the infrared H, K and L bands utilized in the study is given in Table 2. A number of different PSF reference stars were observed, all of which are relatively nearby (typically within about 5° on the sky) and tailored to give roughly similar received counts under various observing configurations. The primary calibrator stars utilized were SAO 186681, SAO 186841, 14 Sgr and HD 165813 although occasionally additional stars were used for confirmatory checks.

In addition to their scientific merit, it is worth noting that the images presented in later sections are a strong testament to the power of aperture masking interferometry in the recovery of high fidelity images. In particular, the pinwheel around WR 104 resolved here possesses strongly asymmetric structure at intermediate dynamic range to the bright core. Deconvolution to obtain at least the full diffraction limit is essential (and ideally, some super-resolution beyond it), as the structure recovered is formally only a few resolution elements across. Seeing conditions over the twelve observing nights found in Table 1 varied over a wide range from extremely poor to very good. Robust, high-fidelity images were recovered

for all epochs and in all filters observed.

This is in contrast to the failure to recover significant reliable structure from the one attempt (we are aware of) to image this target with adaptive optics (Rajagopal et al. 2004). The presence of asymmetric and time-varying extended structure at high resolutions which is nevertheless completely predictable in morphology makes WR 104 almost ideally suited as a “test pattern” target against which imaging experiments may be benchmarked, and we look forward to confirmatory results from new generations of AO instruments.

2.1. K-band images

Images recovered from data taken at 11 separate epochs in the CH4 filter are presented in Figure 1. Although there are 12 observing dates given in Table 1, the first two of 1998 Apr 14 and Apr 15, being separated by only one day, did not give significantly different images and these data have been averaged together for the remainder of this paper. Experience has taught that images recovered from filters within the infrared K-band usually deliver the highest fidelity. The PAHCS filter at longer wavelengths has significantly lower angular resolution with a corresponding loss of detail. On the other hand, the H filter at shorter wavelengths suffers from more severe seeing-induced calibration noise, and furthermore the target star WR 104 is also two magnitudes fainter here than at K (due to the rising IR excess). We therefore begin our discussion of the image morphology with images recovered from the CH4 filter in the K-band, and we later contrast the results from the other filters against this reference.

The images of Figure 1 demonstrate the recovery of extended structures around the bright core with typical image dynamical ranges in excess of 100:1, although higher noise levels due to poor seeing did limit fidelity on occasion (e.g. Jun01 and May04 epochs). The predominant feature at all epochs is a curved plume originating in a bright compact core, and wrapping around a full turn at which point there is a rapid fading in surface brightness to about 1% of the image peak. Beyond the bright first coil, at angular radii $\gtrsim 100$ mas, there can often be seen further windings of a continuing spiral, or in some cases substantial segments of arcs, at a significance at or somewhat above (e.g. Apr98, Jun98) the noise level in each individual image.

The overplotted dashed line on each image in Figure 1 gives the best-fit Archimedian spiral model, which is discussed in greater detail in the following section. Each image has been registered so that the mathematical center of the best-fit spiral (and not the brightest pixel) defines the coordinate origin.

2.2. Archimedian spiral model

An automated procedure was used to extract the coordinates of points lying along the crest of the bright spiral ridges from the images of Figure 1. A model could then be fit to all 11 epochs of data simultaneously. This model consisted of a uniformly-rotating Archimedian spiral, with free parameters: P the rotational period, W the angular expansion (wind) speed, i the inclination to the line-of-sight, ϕ the position angle of i , and θ_0 the position angle of the model at the first epoch (Apr98). There were two additional translational degrees of freedom associated with the registration of the model to the image at each epoch.

With nearly 10 complete rotations of the structure covered by our data series, it was possible to obtain significantly more precise estimates for the model parameters than previously published work. In particular, best-fit models constrained P to be 241.5 ± 0.5 days, a value in very good agreement with the previous best interferometric value (243.5 ± 3 d; Tuthill et al. 2002) and with the reported photometric period (241 d; Kato et al. 2002). The windspeed W was found to be 0.28 ± 0.02 mas/day (or 102 ± 7 mas/yr), also in accord with prior findings (Tuthill et al. 2002). Our best fit for $i = 12^\circ$, although the 1-sigma uncertainty covers a range from $0^\circ - 16^\circ$. Precise constraint of the inclination was hampered by the nearly face-on viewing angle to the system: 12° only results in a 2% distortion of the aspect ratio. Sky orientation parameters were found to be $\phi = 84^\circ \pm 15^\circ$ and $\theta_0 = 269^\circ \pm 1^\circ$.

Despite the fact that the model was only fit to ridge points extracted from the bright inner winding of the spiral, it can be seen from Figure 1 that it also provides a relatively good representation of the structure in the fainter outer regions. This implies that the second winding of the spiral follows closely the expected trajectory from simple expansion, and that the plume remains relatively well defined and compact as it evolves.

A key finding of the modelling study was that the mathematical origin of the best-fit spiral was always systematically offset from the center of the bright core of flux in the images in a highly consistent fashion, as can be seen from Figure 1. This “standoff distance” between the spiral center and brightest pixel was found to be 13.3 ± 1.4 mas which amounted to a rotational displacement downstream along the locus of the spiral of $85^\circ \pm 14^\circ$. Implications for the physical model of the dusty colliding-wind binary from the modelling and imaging presented here are discussed further in later sections.

2.3. H and L-band images

A series of 11 images recovered from H-filter data are presented in Figure 2. Although image fidelity is somewhat lower than for the CH4 filter, the inner bright spiral structure is

well displayed at all epochs. Similarly, Figure 3 shows images recovered from the PAHCS filter from the short-wavelength side of L-band. Data were only collected in this band for the first six epochs of our study (see Table 1), and the resolution obtained is lower than the other filters due to the longer wavelength. The spiral structure of the inner coil is again readily apparent.

Archimedean spiral models were fitted to all H and PAHCS images following the procedure described above. Model parameters such as rotational period and winding angle were found to be in accord with the results from the CH4 filter, however the lower quality of the image data meant that the fits did not significantly advance our knowledge of these properties.

A more profitable strategy for interpretation of the H and PAHCS images was to fix the spiral model parameters P , W , i and ϕ to their values obtained above, and to examine the new data for evidence of systematic changes from this baseline model. One relatively subtle change found was in the mean rotational orientation of the spiral (model parameter θ_0). It was found that the mean rotational displacement of models fitting the H images were retarded by 6° (counterclockwise) while the PAHCS images were found to be advanced by 4° (clockwise) compared to the CH4 reference model. This effect was seen in two independent data-fitting approaches, the first used a similar strategy to that above in fitting to points along ridge crests, while the second entailed the generation of an average CH4 image which was then rotated and fit to each trial H/PAHCS image. The latter procedure was found to be more robust as it was less sensitive to resolution effects which might blur out the exact location of the ridge crest.

A strong note of caution needs to be emphasized here because these relatively small changes in rotation are obtained from comparison between images with differing angular resolutions. In order to investigate the effect of the decline in image resolution going to longer wavelengths H–CH4–PAHCS, simulations were performed in which images were artificially smoothed, and models fit to determine if there were systematic changes in the recovered parameters. Indeed, we found clear and systematic changes of best fit rotation angle, measured to be about 5° in a *counterclockwise* sense when the simulated resolution was degraded to imitate the transitions H–CH4 and CH4–PAHCS. This makes intuitive sense: lowering the resolution tends to blur the center together, and the projecting arm of the spiral *appears* to rotate as more of it is lost to the expanding core. However what is interesting is that this resolution-induced rotational bias is in the opposite sense to the observed *clockwise* rotations of 6° H–CH4 and 4° CH4–PAHCS. It is therefore likely that the true magnitude of this rotation with observing wavelength is underestimated here by a factor of two due to the bias counteracting the signal. However, the fitting of any models to images at the

resolution limit is challenging, and spirals perhaps even more so as due to their self-similar nature. The confirmation and unveiling of detailed substructures within the WR 104 plume must therefore await more powerful telescopes or imaging arrays with still higher angular resolution.

2.4. Lightcurves

Although our imaging experiment was not specifically designed to yield flux measurements, it was possible to extract photometry within our three near-infrared filters to within $\sim 0.1 - 0.2$ mag, although for some nights there were light clouds which compromised the measurement accuracy. These measurements are presented in Figure 4, and show the infrared fluxes to be fairly constant in the H and CH4 filters (to within a few tenths of a magnitude). A larger variation is seen in the PAHCS filter, although it lacks any clear sinusoidal signature with phase and may arise from higher noise levels due to atmospheric contamination (this filter lies near the edge of the infrared L band window).

3. Basic Geometry and Physical Properties

In order to illustrate the physical properties of the WR 104 pinwheel system in the discussions that follow, a cartoon of the basic geometry is given in Figure 5. A pole-on view onto a 20° opening half-angle spiral shock is depicted, together with key elements of the system such as the central binary star, the optically thin inner region of the plume and the dusty first and second coils.

If we are able to measure the physical speed of the dust plume, then this may be combined with the apparent angular velocity to yield the distance to the system. Following Tuthill et al. (1999), if we identify the terminal WR windspeed obtained spectroscopically as $V_\infty = 1\,220$ km/s (Howarth & Schmutz 1992) then we may combine this with our proper motion of 0.28 ± 0.02 mas/day to yield a distance to the system of 2.6 ± 0.7 kpc. By far the dominant error is from the $\sim 25\%$ uncertainty in the windspeed found by comparing the results of different line profile studies (Rochowicz & Niedzielski 1995) (velocities as high as 1 600 km/s have been reported for WR 104 (Torres et al. 1986)).

The distance derived in this fashion is somewhat larger than the 1.6 kpc estimate from possible membership of Sgr OB1 (Lundstrom & Stenholm 1984); a discrepancy which motivated Harries et al. (2004, hereafter HMSK) to question the validity of this method. These authors preferred the smaller distance scale on the basis that the WR wind may be subject

to radiative braking at the OB star (Gayley et al. 1997), and thus the terminal wind velocity may not be representative of the bulk motion of the observed dust plume. It is instructive to pursue this controversy further, for it illuminates some of the unique and interesting properties of these Pinwheel systems.

Let us consider a very simple picture in which we distinguish only 3 populations of gas in the colliding wind system: the free WR wind, the free OB wind, and the material around the shock surface which will contain both, but with modified density and velocity. We will furthermore, for the present, restrict our attention to the hydrodynamic treatment of the inner shock with opening angle given by HMSK. This ignores possible modifications to the shock geometry due to radiative braking, and we devote the Section 4 to a discussion of these effects.

For an ordinary (non-rotating) bowshock system, these populations of gas interact strongly in the heart of the system but at large distances are able to flow more-or-less unimpeded for they occupy distinct regions of space. As the dust is known to form around the colliding-wind interface, the arguments of HMSK would be correct in suggesting a lower velocity for the material in the dust plume from the various braking mechanisms (radiative, shocks).

However, this picture breaks down for the Pinwheel systems when we introduce the rotation of the plume driven by the binary orbit. Recent three-dimensional hydrodynamical simulations of colliding-winds in binary systems which include the coriolis effect have shown strong departures from the simple non-rotating case (Lemaster et al. 2007). Asymmetric shock strengths on the leading and trailing edges of the shock spiral were demonstrated. Although these simulations were mostly concerned with the inner regions of colliding wind systems, there will also be important consequences at large radii which need to be considered for the case of WR 104’s dust plume.

The resultant geometry will be much more complicated because the OB wind will become thoroughly wrapped and entangled within the spherically-expanding WR wind. The interpenetration of the two winds leads to a very different outcome than for the non-rotating case. It is no longer possible for the distinct populations of gas to travel at different speeds without interfering, and in the orbital plane containing the shock, at large radii all populations of gas must collide and eventually come to a common velocity. The two key questions we need to answer to understand the form of the spiral plume are (1) what is this final velocity V_F , and (2) how long will it take until the material in the plume is moving at V_F ?

We may answer (1) with a quantitative discussion of the wind kinetic energy. Following HMSK, for the WR component we adopt a mass-loss rate $\dot{M} = 3 \times 10^{-5} M_{\odot}/\text{yr}$, and a

windspeed $V_{\infty,WR} = 1\,220$ km/s, while for the OB star we have $\dot{M} = 6 \times 10^{-8} M_{\odot}/\text{yr}$ and $V_{\infty,OB} \approx 2\,000$ km/s. The opening angle for the shock can now be calculated from the formula given in Eichler & Usov (1993) to be $\theta = 17.4^{\circ}$ half-angle (rounded to 20° half or 40° full opening angle in HMSK). Note that this explicitly ignores any widening of the opening angle due to radiative braking (see Section 4), but we proceed with this value for the present to ensure consistency with HMSK. At large radii, the solid-angle subtended by the shock cone will be $\Omega = 2\pi(1 - \cos\theta) = 0.03$ sr, so that in the non-rotating case, about 3% of the WR wind and 97% of the OB wind will participate in the collision. We define $R_{bowshock}$ to be the volume ratio of the WR wind involved in the initial bowshock.

In the rotating case, however, a far larger fraction of the WR wind will eventually collide due to the entanglement of the winds. Winds along the two polar axes, with solid angle $\Omega_p = 2\pi(1 - \cos(\pi/2 - \theta)) = 4.1$ sr from the WR can propagate unimpeded. However all gas within an equatorial angular band within $\pm\theta$ from the plane of the orbit must eventually collide with the plume – for our geometry of $\theta = 20^{\circ}$ this corresponds to 34% of the total WR wind. Of this 34%, it is crucial to point out that only $R_{bowshock} = 3\%$ will undergo a ‘prompt’ collision at or just downstream of the shock stagnation point, the remaining 31% will only collide at larger radii as the spiral windings gradually entangle the winds.

If we assume, as seems reasonable for a relatively wide colliding-wind binary, that the shock is mostly adiabatic with little radiative energy loss. The kinetic energy flux of the asymptotic flow for the entangled winds can be found:

$$\frac{1}{2}\dot{M}_F V_F^2 = \frac{1}{2}R_{WR}\dot{M}_{WR}V_{\infty,WR}^2 + \frac{1}{2}R_{OB}\dot{M}_{OB}V_{\infty,OB}^2 \quad (1)$$

Here, R_{WR} and R_{OB} are the fractional volumes of the WR and OB winds that are involved in the collision; from the geometrical arguments above we take $R_{WR} = 0.34$ and $R_{OB} = 1.0$. Substituting values into this equation we calculate that the fast (but tenuous) OB wind will modify the final V_F in the equatorial plane from 1 220 km/s to 1 226 km/s: an insignificant change.

The model may be further refined by adding a third population of radiatively braked material, as suggested by HMSK. Let us suppose (as an upper limit) that *all* WR wind impinging upon the $\theta = 20^{\circ}$ conical shock (3% of the total) is so braked. A preliminary estimate of 800 km/s for V_P the streaming velocity of material in the shock cone has been obtained by fitting to the C III 5696 Å line profile (G. Hill et al., 2007 in preparation). If we add this third population of gas to Equation 1, we obtain $V_F = 1171$ km/s: a decrement of only 4% on $V_{\infty,WR}$. We therefore answer part (1) of our question above that $V_F = V_{\infty,WR}$ with only very minor adjustment, confirming that the momentum-dominant WR wind will

overwhelm other wind populations.

The second part of the question, finding how long will it take for the WR wind to predominate, has a bearing on the shape of the inner spiral: it will be distorted away from Archimedian if the matter is accelerating. A rough estimate can be obtained from a simple “mass loading” argument applied in the equatorial plane of the system. Let us suppose that in the wake immediately behind the OB star, a mass $R_{bowshock} \times \dot{M}_{WR}$ of matter in the plume has a velocity $V_P \ll V_{\infty,WR}$. If material were to continue on this trajectory, after time t it would be overtaken by a mass of the faster wind equal to

$$m = \left(1 - \frac{V_P}{V_{\infty,WR}}\right) \frac{t}{P} R_{WR} \dot{M}_{WR} \quad (2)$$

where P is the orbital period. We may solve this equation for t/P to give the fraction of an orbital period in which a mass of material has collided with the plume from the free WR wind which is equal to that already present from the initial bowshock. Using values from above, we find that 0.1 of an orbital period is sufficient to double the piled-up mass at the inner wall (see Figure 5), and by the time matter has reached the dust formation zone at a quarter turn, it will be strongly ($\sim 70\%$) momentum-dominated by the $V_{\infty,WR}$ wind.

This analysis confirms the general picture that the spiral plume in this system is *rapidly and comprehensively momentum-coupled* to the strong WR wind. The implied distance should therefore be 2.6 ± 0.7 kpc at which the displacement between successive spiral coils is 170 AU, and the excellent match to an Archimedian spiral confirmed. It is very interesting to speculate that the spiral geometry, which allows a far larger interaction between the winds and generates active shocks at much greater radii than a non-rotating system, may also help play a role in the physics of dust nucleation in these systems. Indeed, due to the differing velocities of gasses in the region immediately behind the wake, material will be piled up both at the inner and outer walls (see Figure 5). Numerical simulation in three dimensions of this fascinating ‘twist’ to a conventional bowshock geometry, extending the coriolis force hydrodynamic treatment of Lemaster et al. (2007) to large radii, may prove a valuable guide for further progress in understanding these structures.

4. The Potential Role of Radiative Braking in WR 104

For WR+OB binary systems in which the momentum of the Wolf-Rayet wind substantially exceeds that of the OB star, the WR wind can penetrate very deeply into the acceleration region of the OB-star wind, and in such cases it becomes relevant to consider the role of the OB-star *light* in providing the momentum balance against the WR wind.

The analysis by Gayley, Owocki, & Cranmer (1997, hereafter GOC) suggests that this can lead to a “sudden radiative braking” of the WR wind that can hold the stagnation point along the line of centers farther off from the OB star. This could also modify the angle for the global wind interaction cone, with ramifications for the observations of dust formation. GOC further provide scaling relations to identify whether such radiative braking is likely to be of importance for any given system, and even provide a diagram (their figure 5) to classify several of the known close WR+O binary systems. Let us now apply these criterion to ascertain the potential role of radiative braking for WR 104.

Note first that the systems identified by GOC as likely to have radiative braking are mostly relatively close binaries with periods on the order of days or weeks, and separations of only a few OB-star radii. For wider systems, spherical expansion dilutes the WR wind more strongly in the region around the OB-star, making it easier for the OB-star wind to maintain a standard wind-wind ram pressure balance. But if the WR/OB wind momentum ratio,

$$P_{WR/OB} \equiv \frac{\dot{M}_{WR}V_{WR}}{\dot{M}_{OB}V_{OB}}, \quad (3)$$

is sufficiently high, then even in a relatively wide system, such as WR 104, the standard ram pressure balance could potentially be supplanted by radiative braking. The model wind parameters for WR 104, from Section 3, do indeed imply an extreme momentum ratio, $P_{WR/OB} \cong 305$, and so even the relatively wide separation of $D \cong 2.4$ AU, or $d \equiv D/R_{OB} \cong 50$ OB-star radii, might still induce radiative braking prior to achieving the hydrodynamical stagnation of the winds.

4.1. Estimating the braking radius in WR 104

The following discussion makes use of a number of parameters that are described in greater detail in GOC; for convenience here we provide a brief glossary introducing significant quantities. Radiative acceleration is assumed proportional to η which is found from the effective opacity due to the integral of the forest of spectral lines in the wind. The parameter α was introduced by Castor et al. (1975) to describe how sensitively the line force increases with wind acceleration. GOC found it convenient to define normalized quantities for radiative braking separation d_{rb} and momentum ratio P_{rb} which could be used to scale the actual separation and momentum ratio to gauge the significance of braking in individual cases (see GOC for detailed derivations).

To locate WR 104 on the GOC figure 5 classification diagram, this wind momentum ratio $P_{WR/OB}$ and separation d must be further scaled by associated radiative braking values,

P_{rb} and d_{rb} . To determine those, we first need to evaluate the parameter η , given by GOC eqn. (29), which unfortunately includes an undefined parameter v_* (for that parameter, see Gayley, Owocki, & Cranmer 1996). Reconstruction of the GOC analysis leads to

$$\eta = \frac{1}{\alpha^{\alpha/(1-\alpha)} (1 + \alpha)} \left(\frac{L_{OB}}{L_{WR}} \right)^{1/(1-\alpha)} \frac{2GM_{WR}}{V_{WR}^2 R_{OB}} = \frac{4}{3} \left(\frac{L_{OB}}{L_{WR}} \right)^2 \left(\frac{V_{esc,WR}}{V_{WR}} \right)^2 \frac{R_{WR}}{R_{OB}}, \quad (4)$$

where the latter equality applies to the simple case that the power index $\alpha = 1/2$, and also recasts the scaling in terms of the ratio of WR wind speed to surface escape speed. Note that, in addition to replacing the undefined v_* , this formulation has the advantage of being manifestly independent of the separation D , as required by GOC eqns. (11), (12), and (17).

Applying the wind parameters from Section 3, we find (assuming $\alpha = 1/2$) that for WR 104, $\eta \cong 1.65$. Plugging this into GOC eqn. (30) then leads to $d_{rb} \cong 2.1$. For a standard velocity index $\beta = 1$, we then further find $P_{rb} \cong 0.642$. Using these with the above values for $P_{WR/OB}$ and d , we then find a scaled momentum ratio

$$\hat{P} \equiv \frac{P_{WR/OB}}{P_{rb}} = \frac{305}{0.642} = 475, \quad (5)$$

and scaled separation

$$\hat{d} \equiv \frac{d}{d_{rb}} = \frac{50}{2.1} = 24. \quad (6)$$

In the $\log \hat{P}$ vs. $\log \hat{d}$ plane, systems with radiative braking are defined by the triangular region with both $\log \hat{d} > 0$ and $\log \hat{P} > 2 \log \hat{d}$. The former ensures that the momentum of the OB-star light is sufficient to keep the WR wind from impacting the OB-star surface, and is easily satisfied in this case. The latter condition implies that there can be no normal ram pressure balance between the winds, and thus that radiative braking must stop the WR wind; since for the above parameters, we have $\hat{P} = 475 > 407 = \hat{d}^2$, implying that this condition is also satisfied, although more marginally. If, for example, the estimated wind momentum ratio were reduced by more than about 15%, or the separation were increased by more than about 7%, then the system would no longer satisfy this latter condition. In those cases, a normal ram-pressure balance is still allowed, but even then radiative braking can play a role if the braking radius is outside the wind-wind balance radius.

From GOC eqn. (18), we find that the braking radius for the above standard parameter set is

$$r_b = x_b D = \frac{D}{1 + (d/\eta)^{1/3}} = 0.254 D = 12.1 R_{OB}. \quad (7)$$

For comparison, for the simple case of constant flow speed (i.e. velocity power index $\beta = 0$), ram pressure balance in the absence of direct radiative forces occurs at a radius (cf. GOC

eqn. (2))

$$r_s = x_s D = \frac{D}{1 + \sqrt{P_{WR/OB}}} = 0.054 D = 2.6 R_{OB}. \quad (8)$$

For such a purely hydrodynamical balance, a global momentum analysis (Canto, Raga, and Wilkin 1996; Gayley & Owocki in preparation) yields a transcendental relation between the cone-opening half-angle θ_s and the momentum ratio $P_{WR/OB}$,

$$\tan \theta_s - \theta_s = \frac{\pi}{P_{WR/OB} - 1}. \quad (9)$$

For large momentum ratio $P_{WR/OB} \gg 1$, use of a small-angle approximation for $\tan \theta_s \cong \theta_s + \theta_s^3/3$ gives the asymptotic form,

$$\theta_s \cong \left(\frac{3\pi}{P_{WR/OB}} \right)^{1/3}; \quad P_{WR/OB} \gg 1. \quad (10)$$

To recover $\theta_s = 90^\circ$ for the symmetric momentum case $P_{WR/OB} = 1$, we can write a more generally applicable approximate solution, accurate to within about 6% for all $P_{WR/O}$,

$$\theta_s \cong \frac{121}{31/90 + P_{WR/OB}^{1/3}} \quad (11)$$

where using $121 = (180/\pi) (3\pi)^{1/3}$ gives this angle in degrees.

For our estimate of $P_{WR/OB} = 305$ for WR 104, we then obtain $\theta_s \cong 18^\circ$, in good agreement with the value from Section 3 derived from the heuristic formula of Eichler & Usov (1993).

4.2. Radiative force influence on the shock-cone angle

An important question is then, by how much can the effects of radiative forces from the OB star potentially widen this shock cone? Only a complete simulation can answer this definitively, but we can make conceptual progress using heuristic approximations to attempt to better constrain the circumstances under which we should expect an important radiative modification of the bow shock geometry. Two approaches that borrow from the existing sudden radiative braking analysis can be termed the ‘‘Global Momentum Augmentation’’ (GMA) and the ‘‘Radiative Wall’’ (RW) approach. Each gives similar results for the opening angle, and so here we briefly outline just the former, deferring to Gayley & Owocki (in preparation) for a detailed discussion of both approaches.

In the GMA approach, the radiation interaction with the incident WR wind is assumed to augment the OB-star wind momentum flux by a globally constant factor, set by the requiring that the stagnation point of the combined effective momentum fluxes equal the braking radius in eqn. (7). We write this factor as $\gamma\tau$, where γ is the ratio of the OB-star radiative momentum flux to its wind momentum flux, $L_{OB}/\dot{M}_{OB}v_{OB}$, and τ is an optical-depth-like parameter that simulates the coupling of the OB radiative momentum flux to the WR wind. In analogy to the global analysis cited above (Gayley & Owocki, in preparation), we find for the large momentum ratio limit,

$$\theta_s \cong 121 \left(\frac{1 + \gamma\tau}{P_{WR/OB}} \right)^{1/3}. \quad (12)$$

In this scenario radiative braking would alter the shock geometry whenever $\gamma\tau$ is appreciable, and since γ in WR 104 is expected to be large, this is not a terribly restrictive requirement for the coupling parameter τ . Since the braking radius r_{rb} scales roughly with $\eta^{-1/3}$ when braking is important, the condition that the effective momentum ratio used in r_s be reduced enough to achieve $r_{rb} = r_s$ (see eqs. [7] and [8]) is tantamount to requiring

$$\gamma\tau \cong \left(\frac{\eta R_{OB}}{D} \right)^{2/3} P_{WR/OB}. \quad (13)$$

This implies a shock opening angle

$$\theta_s \cong 121 \left(\frac{\eta R_{OB}}{D} \right)^{2/9}, \quad (14)$$

which for $\eta = 1.65$ and $D/R_{OB} = 46.5$ evaluates to $\theta_s \cong 58^\circ$, representing a factor ~ 3.2 increase over the purely hydrodynamic value $\theta_s \cong 18^\circ$. This may be a significant overestimate, because of the optimistic assumptions made about the radiative momentum coupling, but it demonstrates that radiative braking could indeed increase the shock cone opening if the WR wind opacity continues to be high throughout the flow.

A similar result can be reached through the radiative wall approach. Although both approximations are too heuristic to be considered quantitatively reliable, they do suggest that strong radiative braking for the assumed parameters in WR 104 should be expected to widen the bow shock angle considerably, possibly by a factor of 2 or more when compared to the purely hydrodynamic result $\theta_s \cong 18^\circ$, as long as the incident WR wind maintains the same high levels of opacity for the OB starlight that it must have had to have been radiatively driven from the WR star. This assumption is currently of unknown validity, and indeed if we take the opposite limit, and say that the line-opacity is just what is needed

to drive the relatively weak OB-star wind, then radiative braking will be *much* weaker and would not likely alter the shock-cone geometry in any measurable way.

To address intermediate values of the effective WR wind opacity, recalling that η , for fixed α , is simply proportional to the integrated spectrum-weighted line opacity distribution with no regard to optical depth (i.e., self-shadowing) corrections. Thus one may either make assumptions about this line opacity to predict η , or one may use observations of the bow shock cone to infer η and reason to conclusions about the line distribution. Further analysis will be required to constrain these expectations more quantitatively, but it seems at least plausible that radiative braking may be important in the wind-wind interaction and shock-cone geometry of WR 104, *if* the line opacity of the WR wind interacting with the OB starlight is substantially enhanced above what is needed to drive the OB-star wind itself. Reversing the logic, it may be concluded that evidence for a significant widening of the bow-shock cone relative to what may be explained hydrodynamically may be interpreted as evidence that the WR wind does indeed carry with it an intrinsically high opacity when it impinges into the region of strong OB-star radiative flux.

Our images of the WR 104 plume are able to rule out some of the more extreme enlargements to the cone opening angle in the above scenarios. Fits to the data by HMSK found that model cone half-angles of 40° or greater (twice the hydrostatic value) were rejected. With still higher angular resolutions than those obtained here, it should be possible to get a direct measurement of the cone opening angle from the images, revealing the role played by radiative braking on the shock geometry.

5. The Profile of the Spiral Plume

Using the excellent fits provided by the theoretical spiral locus to the observed plume of emission from Figures 1, 2 & 3, an investigation of the brightness profile along the length of the dust plume was performed. The flux, summed over a band following the model spiral, was accumulated over all images recovered. Average profiles, plotted as a function of angular displacement along the spiral, are given in Figure 6 for all three filter bandpasses. Also overplotted is the same profile along the spiral calculated from the synthetic radiative-transfer images of HMSK. All experimental curves follow a similar form (with some departures for PAHCS which we attribute to the systematically lower resolution) exhibiting a steep rise in flux from the spiral center to a point about 90° downstream followed by a rapid drop as the bright core of the system is traversed. There now follows a region of roughly monotonic decline between about $150 - 400^\circ$, at which point there is a very sharp drop in brightness flattening to level of less than 1% of the peak for the second coil (CH4 filter only).

The initial sharp rise in flux seen in Figure 6 gives another way to visualize the “standoff distance” between the spiral center and brightest pixel, measured earlier to be 13.3 ± 1.4 mas or $85^\circ \pm 14^\circ$ downstream along the spiral. Given the 241.5 d period, this corresponds to a kinematic age for the material of 57 ± 10 d. This value is in remarkable agreement with the value of ~ 58 – 87 d for the delay between periastron passage and the peak in the dust production in the well-studied episodic colliding-wind binary dust producer WR 140 (Williams et al. 1990; Marchenko et al. 2003). The finding that the peak in dust production occurs at some distance downstream from the colliding-wind stagnation point (~ 30 AU for WR 104) points to a more complicated picture for dust formation physics in colliding-wind binaries than the simple shock compression/cooling models (Usov 1991). A number of avenues for additional physics have been presented (see also Crowther 2003), with one likely element being escape from the dust-hostile immediate circumstellar radiation environment. Chemical seeding of the WR wind (predominantly helium) with hydrogen from the OB star at the contact surface may help to enhance dust formation pathways (Le Teuff 2002), although such mixing may not be very rapid. Shielding from the intense radiation field does appear to be a key ingredient, and sets the playing field for sharply nonlinear grain growth in which small clumps may self-shadow larger areas downstream in a runaway process. Recent numerical simulations of colliding flows have shown that matter is squeezed into thin high-density shells threaded by still higher density filaments as a result of supersonic turbulence (Walder & Folini 2000). It was suggested these conditions can persist for a considerable time in the flow before dissipation by internal shocks and vortex cascades. Further to these earlier ideas, we now also add the idea of wind entanglement which can generate significant shock activity well downstream of the nose, as discussed in earlier sections. Whatever mix of these or other elements may go into the next generation of colliding-wind dust formation models, there certainly seems scope to address the outstanding issue of whether the dusty-WC phenomena has a necessary link to binarity (Monnier et al. 1999; Williams & van der Hucht 2000; Monnier et al. 2007), or whether novel dust formation pathways in an isolated wind may also be important in some circumstances (Zubko 1998; Cherchneff et al. 2000).

After the peak at 85° , the profiles of Figure 6 exhibit a steady decline (but note the logarithmic y-axis). This is in accord with the relatively flat temperature profile found in models of the centrally-illuminated dust spiral models of HMSK, although the bright peak near the heart of the system is not reproduced in the simulations. A fairly detailed comparison between the radiative transfer results and published masking images of WR 104 can be found in HMSK, although our new results here highlight some discrepancies which we hope will motivate future refinements. The flux level of the second winding of the spiral is well reproduced at the beginning (480° – 600°) but the secondary bright knot in the model tail seen at 2 complete turns was not observed in the data. Although a detailed comparison

is beyond the scope of the present paper, one possible implication is that the optical depth of the dust in the model is not high enough in the core of the system. Increasing it may help to generate the bright peak at 85° , and at the same time decrease the illumination on the second coil therefore suppressing the spurious feature at 720° .

The very sharp decline in flux between $400\text{--}480^\circ$ is a result of the shadow cast by the first winding of the spiral onto the second, causing a rapid drop in temperature for the eclipsed material. This feature has been commented upon since the discovery of the pinwheels (Tuthill et al. 1999), and was also reproduced in radiative transfer models (HMSK). What is particularly interesting is that the terminator is found at an angular ordinate of $\sim 440^\circ$ along the spiral, or about 80° beyond one complete revolution. This extra angular displacement (easily visualized in the figure as the full revolution 360° location has been marked) gives further independent confirmation for the existence and size of the optically thin inner cavity surrounding the central stars. We refer the reader back to Figure 5 for an easily understood and intuitive depiction of the angular locations of the inner optically thin plume, and the geometry of the shadow cast upon the second coil by the first.

Also of interest in helping to constrain future generations of dust plume models are the multi-wavelength observations of the spiral given in Figures 1, 2 & 3. In particular, there was a systematic rotational displacement found with observing wavelength with a (lower limit) position angle of 6° from H–CH₄ and 4° from CH₄–PAHCS (true values may be a factor of ~ 2 larger – see discussion in Section 2.3). This implies that the transverse temperature profile of the plume can be explored by our high resolution techniques. Short wavelength observations will preferentially weight the hottest material on the inner edge of the plume facing the central stars, while longer wavelengths will give a better indicator of the bulk concentration of warm dust. Again, we must defer detailed modelling of these effects to a future paper, but note that preferential radiative heating of the inner wall was predicted in models of HMSK. An alternate scenario is that of asymmetric heating by shocks of differing strength at the inner and outer walls, as recently demonstrated in the rotating hydrodynamic simulations of Lemaster et al. (2007).

6. Geometrical Implications of the Plume Structure

A key finding from earlier studies of the WR 104 pinwheel has been the low eccentricity of the orbit of the central stars (Tuthill et al. 1999, 2002). As noted earlier (Monnier et al. 1999), this finding may be a “smoking gun” pointing to previous episodes of tidal circularization and likely Roche-lobe interactions with possible mass transfer and/or envelope stripping. Such an event provides one of the two possible pathways to the creation of a

Wolf-Rayet (Paczynski 1967); the other being strong wind-driven mass loss in a single star (Chiosi et al. 1978). With our long time-sequence of observations sampling all phases of the orbit, we are able to put tight constraints on the allowed levels of orbital eccentricity in the case of WR 104. Although it would be possible to fit eccentric spiral models directly to the data, we favored a more indirect approach as for small to moderate levels of eccentricity, the departure in shape from an Archimedian spiral was subtle. The most easily detectable effect that an eccentric orbit has in perturbing the rotating spiral model away from its ideal form will be in departures from a constant rate of rotation.

We have therefore performed a careful fit of the best-fit orientation of the spiral structure at each epoch, and compared the values obtained with the model of a simple, constant angular velocity. This was done in two different ways which gave similar results: firstly by fitting to points extracted from the crest of the bright spiral ridge, and secondly by fitting each full image to a mean template. The uniformity of the angular rotation rate extracted from the real data, which is given in in Figure 7, was then compared with results from model simulations. A family of synthetically-generated spiral images of varying eccentricity were fit in an identical fashion to the real data, allowing us to derive quantitative limits on the levels of eccentricity present in the WR 104 orbit. Figure 7 shows the rotational uniformity from the data and examples from two of the synthetic eccentric model images. The rotation is seen to be highly uniform, ruling out all but very modest eccentricities. A 2σ upper limit of $e \lesssim 0.06$ was obtained in this fashion.

Having thus established the properties of the best-fit uniform Archimedian spiral model, it was then possible to generate a stacked composite image averaging over all epochs of data taken in the CH4 filter. Individual data frames were corrected for inclination on the sky (simulating a perfectly face-on view) and de-rotated to coincide with the first (Apr98) epoch before being co-added. A composite image, displaying significantly greater dynamic range than any of the single-epoch images from Figure 1, is given in Figure 8. Variations in morphology between different epochs beyond those expected from the rotating spiral model are minor, and all appear to be within the noise level of the image recovery process. We therefore hope that this image, as a mean over all epochs, may provide a resource to modellers and others interested in the best possible snapshot of the geometry of these pinwheel systems.

The flat infrared lightcurves of Figure 4 discussed above affirm the status of WR 104 as a “constant” dust-producer (Williams 1997), yet stand in contrast to the large 2.7 mag “quasi-periodic” variability (periodic component $\gtrsim 1$ mag) in the visible lightcurves reported by Kato et al. (2002). With a narrow cone half-angle (20° ; HMSK), face-on orientation to the line of sight and very low levels of orbital eccentricity, the spiral dust plume gives no obvious mechanism for modulating the visible flux from this system. The lack of detectable

infrared variation argues for steady and constant dust production at all orbital phases, with minimal effects from any inclination to the the line of sight. Visible light scattered from the dust plume may be more strongly modulated by rotation and inclination effects, however it is difficult to see how variations in the V lightcurve as large as $\gtrsim 1$ mag could arise from this. Possible scenarios include opacity effects from gas (or possibly small quantities of dust) associated with the innermost regions of the shock cone which modulate the light of the OB star, line-of-sight (polar-axis) dust creation independent of the colliding wind mechanism, or some geometrical effect from a sharp opacity gradient possibly created at an earlier phase (further discussion can be found in Kato et al. 2002).

7. WR Systems as Supernova Progenitors

As a final point of discussion, we also explore the implications of future evolution of this system with particular regard to the face-on viewing angle to Earth. The formal Archimedian spiral fits yielded an inclination $i = 12^\circ$, but for such a small angle to the line-of-sight the uncertainty was large and fully consistent with the range from $0^\circ - 16^\circ$. A further source of uncertainty arises from the limitations of the simple two-dimensional spiral model used. In reality, the pinwheel is of course a three-dimensional structure which may present us with more complicated opacity effects such as limb-brightening. If we consider a single circular cross-section through the conical shock, as this is carried downstream by the WR wind, it will become inflated and distorted by the spherical expansion into an elongated “D”. Eventually at large radii, the plume shape will resemble an equatorial band wrapped around a sphere, subtending an angle equal to that of the shock cone. This underlying spherical geometry gives rise to a fundamental insensitivity to the line-of-sight inclination: modest changes of tilt for such a structure result in only a very small or zero change in observed aspect ratio. For these reasons, our upper limit of 16° may be an underestimate. Firmer constraint of the inclination from the data presented here would require detailed radiative transfer modelling with varying lines of sight onto a three-dimensional structure.

Despite these quantitative caveats, it remains apparent that in WR 104, Earth has an approximately pole-on view onto a relatively nearby, massive WR binary system. Given the prehistory of mass transfer and envelope-stripping suggested above, it therefore seems likely that Earth also lies in the polar direction with respect to the spin axis of both WR and OB stars due to the prior angular momentum evolution of such binary systems (e.g. Zahn 1977; Tassoul 1987). As both objects in the system should eventually explode as core-collapse supernovae, it is interesting to speculate on how our “privileged” polar vantage point may affect our experience of this event, which should happen within a timescale of

several hundred thousand years for the WR component (Maeder 1981; Chiosi & Maeder 1986). It is becoming more accepted that all supernova explosions probably exhibit some preferred axis aligned with the progenitor stellar spin. As one of the closest imminent WC-class Wolf-Rayets, an isotropic supernova in WR 104 at kiloparsec scale distances would no doubt put on an impressive show, but any impact on Earth’s biosphere is likely to be negligible (Ellis & Schramm 1995). However for a highly *anisotropic* explosion, the most extreme example of which would be a Gamma Ray Burst, effects could be significant if Earth lies within the $\lesssim 12^\circ$ opening angle (Frail et al. 2001) of the burst, even at 2kpc distances (Melott et al. 2004; Thomas et al. 2005a,b).

Could WR 104 produce a GRB? Certainly a case could be made that the OB component of the binary system, which was the recipient of mass and angular-momentum transfer in the prior Roche-lobe overflow event, may meet the requirements for envelope mass and angular momentum for many current models of GRB formation (see Petrovic et al. 2005, for a discussion of WR binaries as GRB progenitors). The Wolf-Rayet component, with WC spectral type, has arguably the shortest fuse, being in the last known stable phase before supernova. Although prior stripping may have lowered the envelope mass into a regime less favorable for conventional collapsar GRB’s, there are also more exotic magnetar (millisec pulsar driven) GRB models which may prove viable (Gaensler et al. 2005; Metzger et al. 2007). In short, this is a very active and rapidly-evolving field, and the uncertainties outnumber the firm conclusions in arriving at a mass/metallicity/evolutionary portrait of likely GRB progenitors. Whether or not the WR 104 system will play host to a future GRB, it does seem clear that two pole-oriented supernovae will occur, and that energy and matter will be preferentially ejected along this axis (see Fryer & Warren 2004, for a discussion of the effects of stellar rotation on SN explosions). Further observations to constrain the inclination of the orbital plane, which should be possible with spectroscopic monitoring, are therefore encouraged.

The data presented herein were obtained at the W.M. Keck Observatory, which is operated as a scientific partnership among the California Institute of Technology, the University of California and the National Aeronautics and Space Administration. The Observatory was made possible by the generous financial support of the W.M. Keck Foundation. The Authors would like to particularly thank the instrument technicians and engineering crew at the observatory for their help and support of our unorthodox observing techniques. Devinder Sivia kindly provided the maximum entropy mapping program “VLBMEM”, which we have used to reconstruct our diffraction limited images. This work has been supported by grants from the National Science Foundation and the Australian Research Council. We thank Charles Townes for his long-standing support of this program, and Bryan Gaensler, Shami Chatterjee and Grant Hill for helpful discussions.

REFERENCES

- Bethe, H. A. 1990, *Reviews of Modern Physics*, 62, 801
- Canto, J., Raga, A. C., & Wilkin, F. P. 1996, *ApJ*, 469, 729
- Castor, J. I., Abbott, D. C., & Klein, R. I. 1975, *ApJ*, 195, 157
- Cherchneff, I., Le Teuff, Y. H., Williams, P. M., & Tielens, A. G. G. M. 2000, *A&A*, 357, 572
- Chiosi, C., Nasi, E., & Sreenivasan, S. R. 1978, *A&A*, 63, 103
- Chiosi, C., & Maeder, A. 1986, *ARA&A*, 24, 329
- Crowther, P. A. 1997, *MNRAS*, 290, L59
- Crowther, P. A. 2003, *Ap&SS*, 285, 677
- Danchi, W. C., Tuthill, P. G., & Monnier, J. D. 2001, *ApJ*, 562, 440
- Eichler, D., & Usov, V. 1993, *ApJ*, 402, 271
- Ellis, J., & Schramm, D. N. 1995, *Proceedings of the National Academy of Science*, 92, 235
- Frail, D. A., et al. 2001, *ApJ*, 562, L55
- Fryer, C. L., & Warren, M. S. 2004, *ApJ*, 601, 391
- Gaensler, B. M., McClure-Griffiths, N. M., Oey, M. S., Haverkorn, M., Dickey, J. M., & Green, A. J. 2005, *ApJ*, 620, L95
- Gayley, K. G., Owocki, S. P., & Cranmer, S. R. 1997, *ApJ*, 475, 786
- Gayley, K. G., Owocki, S. P., & Cranmer, S. R. 1996, *Workshop on Colliding Winds in Binary Stars to Honor Jorge Sahade*, vol. 5, p. 68, 68
- Gull, S.F. and Skilling, J. 1984, *Proc. IEEE*, 131, 6
- Haniff, C. A., & Buscher, D. F. 1992, *J. Opt. Soc. Am. A*, 9, 203
- Harries, T. J., Monnier, J. D., Symington, N. H., & Kurosawa, R. [HMSK] 2004, *MNRAS*, 350, 565
- Högbom, J. 1974, *ApJS*, 15, 417

- Howarth, I. D., & Schmutz, W. 1992, *A&A*, 261, 503
- van der Hucht, K. A. 2001, *New Astronomy Review*, 45, 135
- Ireland, M. J., Monnier, J. D., & Thureau, N. 2006, *Proc. SPIE*, 6268,
- Kato, T., Haseda, K., Yamaoka, H., & Takamizawa, K. 2002, *PASJ*, 54, L51
- Kuiper, G. P. 1941, *ApJ*, 93, 133
- Lemaster, M. N., Stone, J. M., & Gardiner, T. A. 2007, *ApJ*, 662, 582
- Le Teuff, Y. H. 2002, *Interacting Winds from Massive Stars*, 260, 223
- Lundstrom, I., & Stenholm, B. 1984, *A&AS*, 58, 163
- Maeder, A. 1981, *A&A*, 99, 97
- Marchenko, S. V., Moffat, A. F. J., Vacca, W. D., Côté, S., & Doyon, R. 2002, *ApJ*, 565, L59
- Marchenko, S. V., & Moffat, A. F. J. 2006, *ArXiv Astrophysics e-prints*, arXiv:astro-ph/0610531
- Matthews, K., Ghez, A. M., Weinberger, A. J., & Neugebauer, G. 1996, *PASP*, 108, 615
- Mauron, N., & Huggins, P. J. 2006, *A&A*, 452, 257
- Marchenko, S. V., et al. 2003, *ApJ*, 596, 1295
- Melott, A. L., et al. 2004, *International Journal of Astrobiology*, 3, 55
- Metzger, B. D., Thompson, T. A., & Quataert, E. 2007, *ArXiv e-prints*, 704, arXiv:0704.0675
- Mondal, S., & Chandrasekhar, T. 2002, *MNRAS*, 334, 143
- Monnier, J. D., Tuthill, P. G., & Danchi, W. C. 1999, *ApJ*, 525, L97
- Monnier, J. D., Tuthill, P. G., & Danchi, W. C. 2000, *ApJ*, 545, 957
- Monnier, J. D., Greenhill, L. J., Tuthill, P. G., & Danchi, W. C. 2002, *ApJ*, 566, 399
- Monnier, J. D., Tuthill, P. G., & Danchi, W. C. 2002, *ApJ*, 567, L137
- Monnier, J. D., et al. 2004, *ApJ*, 605, 436

- Monnier, J. D., Tuthill, P. G., Danchi, W. C., Murphy, N., & Harries, T. J. 2007, *ApJ*, 655, 1033
- Moran, J. A., & Reichart, D. E. 2005, *ApJ*, 632, 438
- Paczynski, B. 1967, *Acta Astronomica*, 17, 355
- Pauls, T. A., Young, J. S., Cotton, W. D., & Monnier, J. D. 2005, *PASP*, 117, 1255
- Petrovic, J., Langer, N., Yoon, S.-C., & Heger, A. 2005, *A&A*, 435, 247
- Rajagopal, J. K., Barry, R., Lopez, B., Danchi, W. C., Monnier, J. D., Tuthill, P. G., & Townes, C. H. 2004, *Proc. SPIE*, 5491, 1120
- Rochowicz, K., & Niedzielski, A. 1995, *Acta Astronomica*, 45, 307
- Ryder, S. D., Sadler, E. M., Subrahmanyan, R., Weiler, K. W., Panagia, N., & Stockdale, C. 2004, *MNRAS*, 349, 1093
- Sivia, D.S. 1987, Ph.D. diss., Cambridge Univ.
- Stevens, I. R., Blondin, J. M., & Pollock, A. M. T. 1992, *ApJ*, 386, 265
- Struve, O. 1950, *Stellar Evolution*, Princeton University Press, NJ.
- Tassoul, J.-L. 1987, *ApJ*, 322, 856
- Thomas, B. C., et al. 2005a, *ApJ*, 634, 509
- Thomas, B. C., Jackman, C. H., Melott, A. L., Laird, C. M., Stolarski, R. S., Gehrels, N., Cannizzo, J. K., & Hogan, D. P. 2005b, *ApJ*, 622, L153
- Torres, A. V., Conti, P. S., & Massey, P. 1986, *ApJ*, 300, 379
- Tuthill, P. G., Monnier, J. D., & Danchi, W. C. 1999, *Nature*, 398, 487
- Tuthill, P. G., Monnier, J. D., Danchi, W. C., Wishnow, E. H., & Haniff, C. A. 2000, *PASP*, 112, 555
- Tuthill, P. G., Danchi, W. C., Hale, D. S., Monnier, J. D., & Townes, C. H. 2000, *ApJ*, 534, 907
- Tuthill, P. G., Monnier, J. D., Danchi, W. C., Hale, D. D. S., & Townes, C. H. 2002, *ApJ*, 577, 826

- Tuthill, P. G., Monnier, J. D., & Danchi, W. C. 2002, *Interacting Winds from Massive Stars*, 260, 321
- Tuthill, P. G., Men'shchikov, A. B., Schertl, D., Monnier, J. D., Danchi, W. C., & Weigelt, G. 2002, *A&A*, 389, 889
- Tuthill, P. G., Monnier, J. D., Danchi, W. C., & Turner, N. H. 2003, *A Massive Star Odyssey: From Main Sequence to Supernova*, 212, 121
- Tuthill, P., Monnier, J., Tanner, A., Figer, D., Ghez, A., & Danchi, W. 2006, *Science*, 313, 935
- Usov, V. V. 1991, *MNRAS*, 252, 49
- Walder, R., & Folini, D. 2000, *Ap&SS*, 274, 343
- Woosley, S. E., Heger, A., & Weaver, T. A. 2002, *Reviews of Modern Physics*, 74, 1015
- Woosley, S. E., & Bloom, J. S. 2006, *ARA&A*, 44, 507
- Vanbeveren, D., De Loore, C., & Van Rensbergen, W. 1998, *A&A Rev.*, 9, 63
- Williams, P. M., van der Hucht, K. A., Pollock, A. M. T., Florkowski, D. R., van der Woerd, H., & Wamsteker, W. M. 1990, *MNRAS*, 243, 662
- Williams, P. M. 1997, *Ap&SS*, 251, 321
- Williams, P. M., & van der Hucht, K. A. 2000, *MNRAS*, 314, 23
- Zahn, J.-P. 1977, *A&A*, 57, 383
- Zubko, V. G. 1998, *MNRAS*, 295, 109

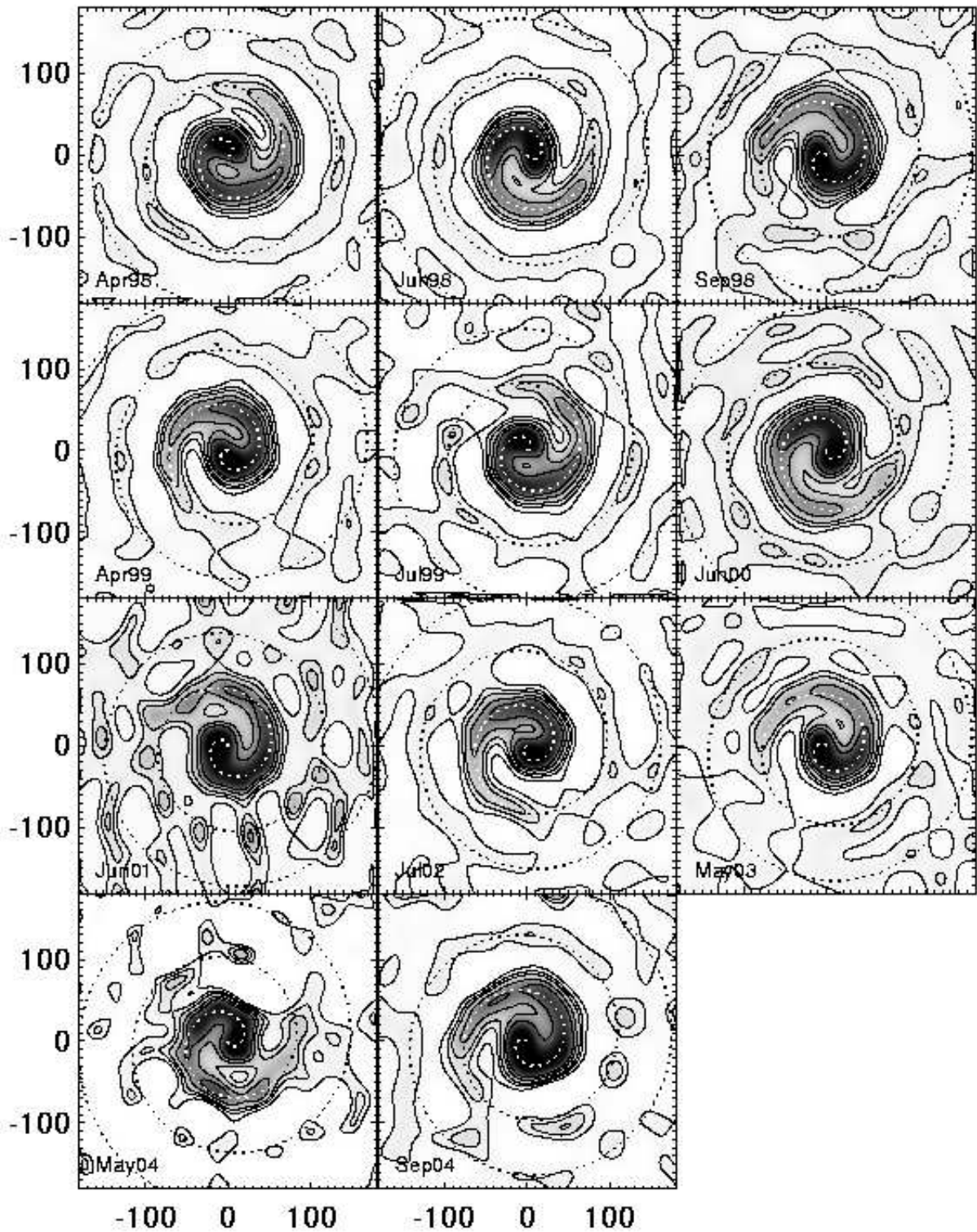


Fig. 1.— Images recovered from data in the CH₄ filter over 11 observing epochs. Contour levels are .4, 1, 2, 5, 10, 50 % of the peak. North (Dec.) is up and east (R.A.) to the left with the image scale labelled in milliseconds of arc. Images have been centered on the mathematical origin of the best-fit Archimedean spiral model (dashed line: see text for details).

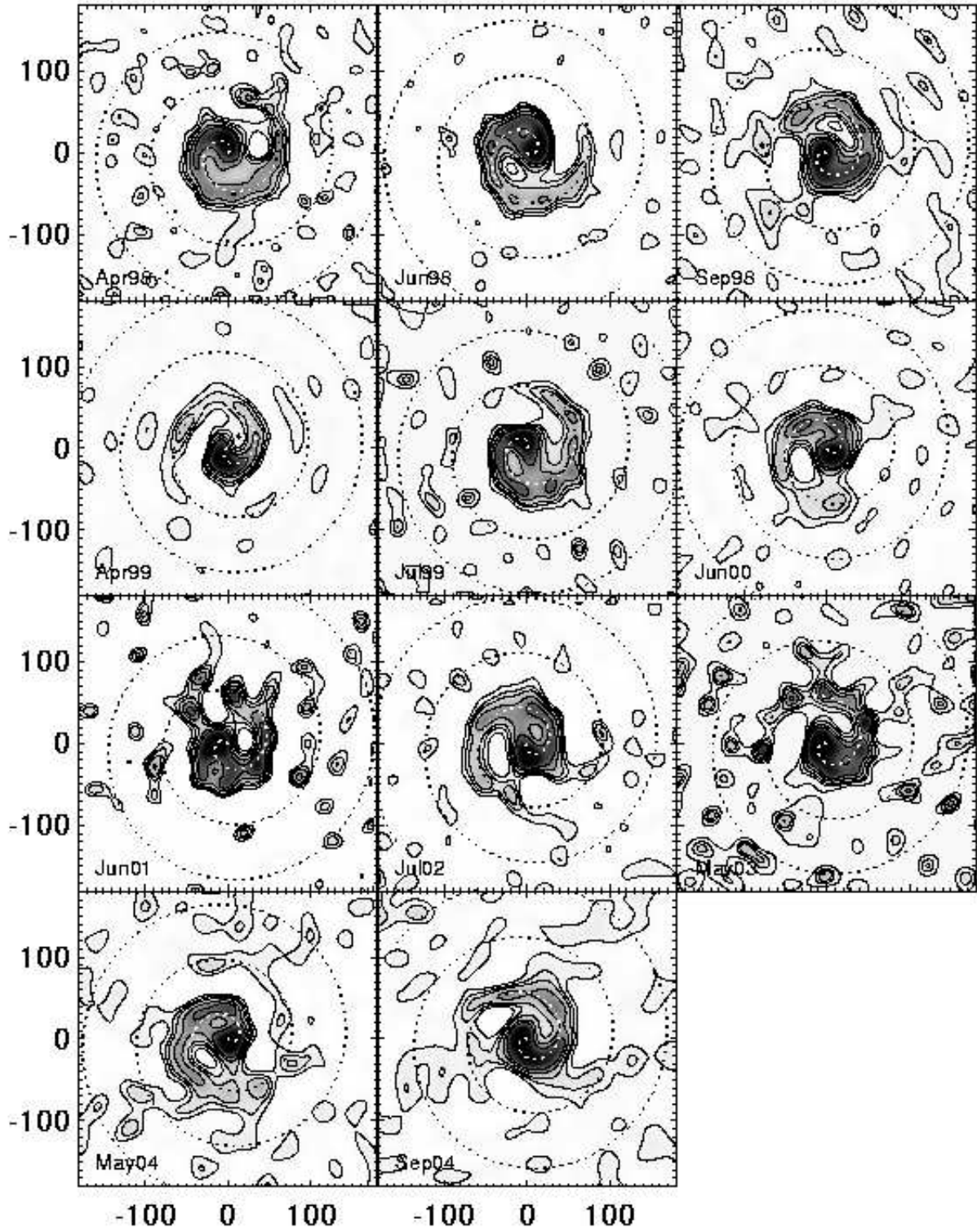


Fig. 2.— Images recovered from data in the H filter over 11 observing epochs. See caption to Figure 1 for details.

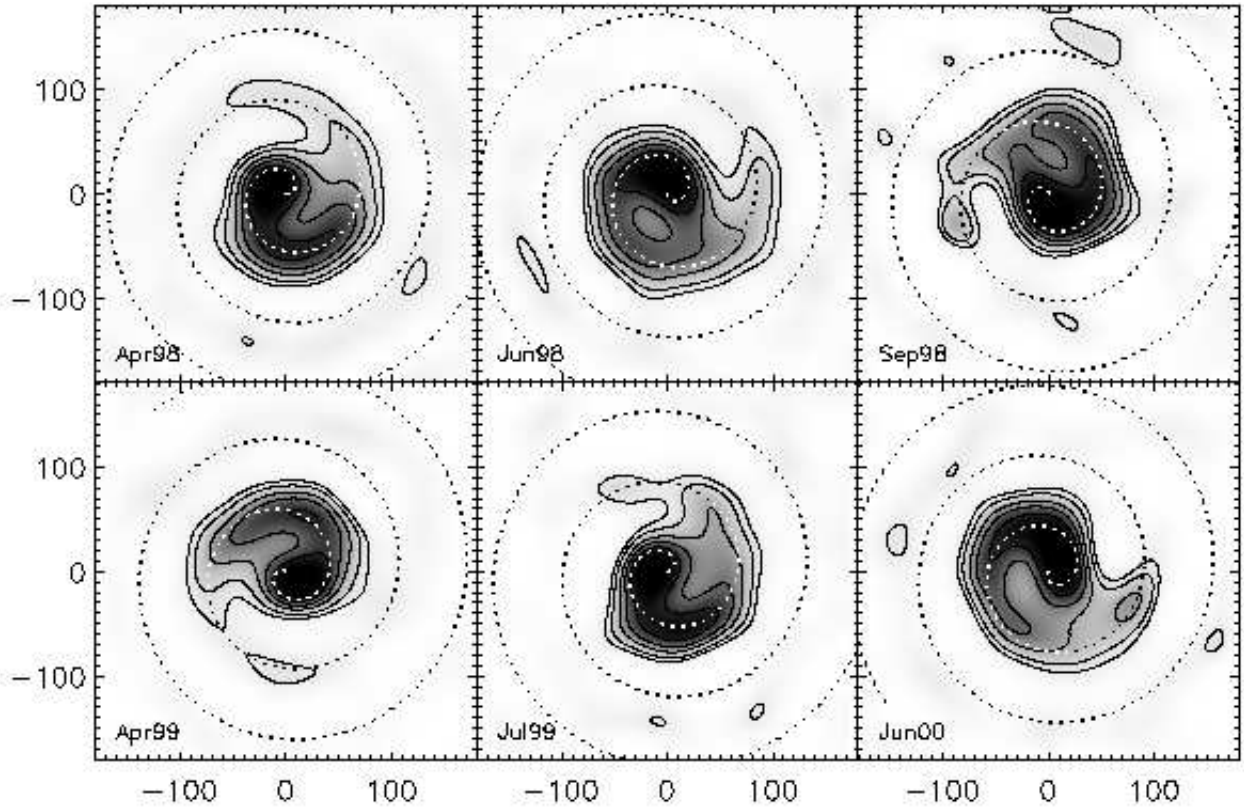


Fig. 3.— Images recovered from data in the PAHCS filter over 6 observing epochs. Contour levels are 1, 2, 5, 10, 20% of the peak. Otherwise similar to Figure 1.

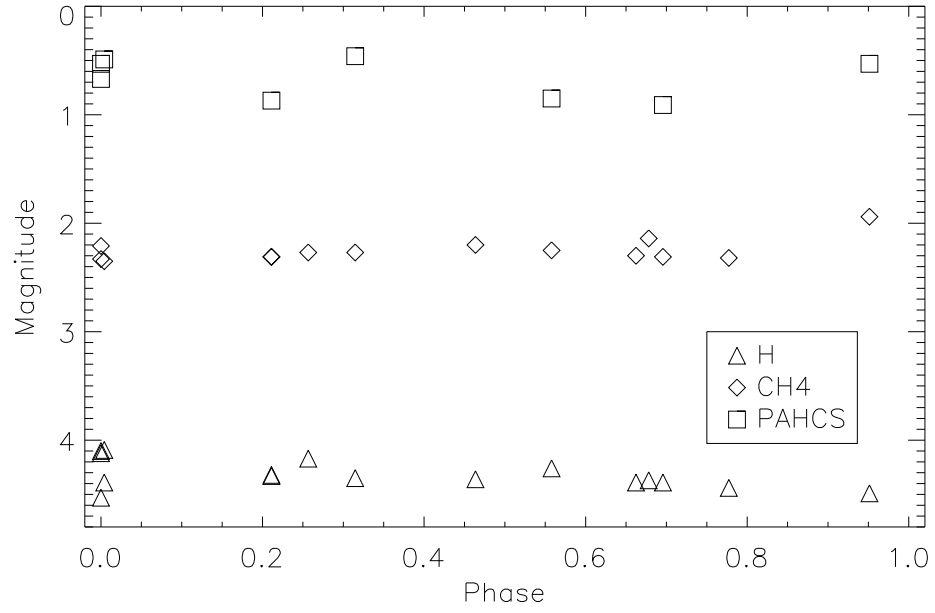


Fig. 4.— Photometry data for WR 104 obtained in our three filter bandpasses (key inset), folded with the 241.5 d period.

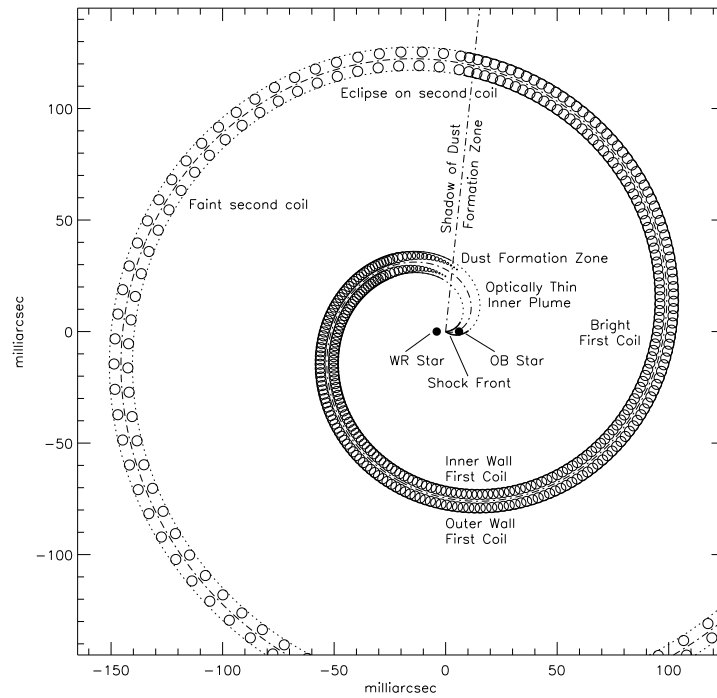


Fig. 5.— Schematic diagram of the key elements in the WR 104 system. The geometry depicted is that of a face-on view onto a 20° cone half-angle pinwheel. The axis of the system, and the line of shadow cast at 84° to the spiral origin ($\theta = 0$), are indicated as dot-dashed lines. Key elements are labeled, and some, such as the binary separation, are not to scale (depicted here about a factor of ten too large).

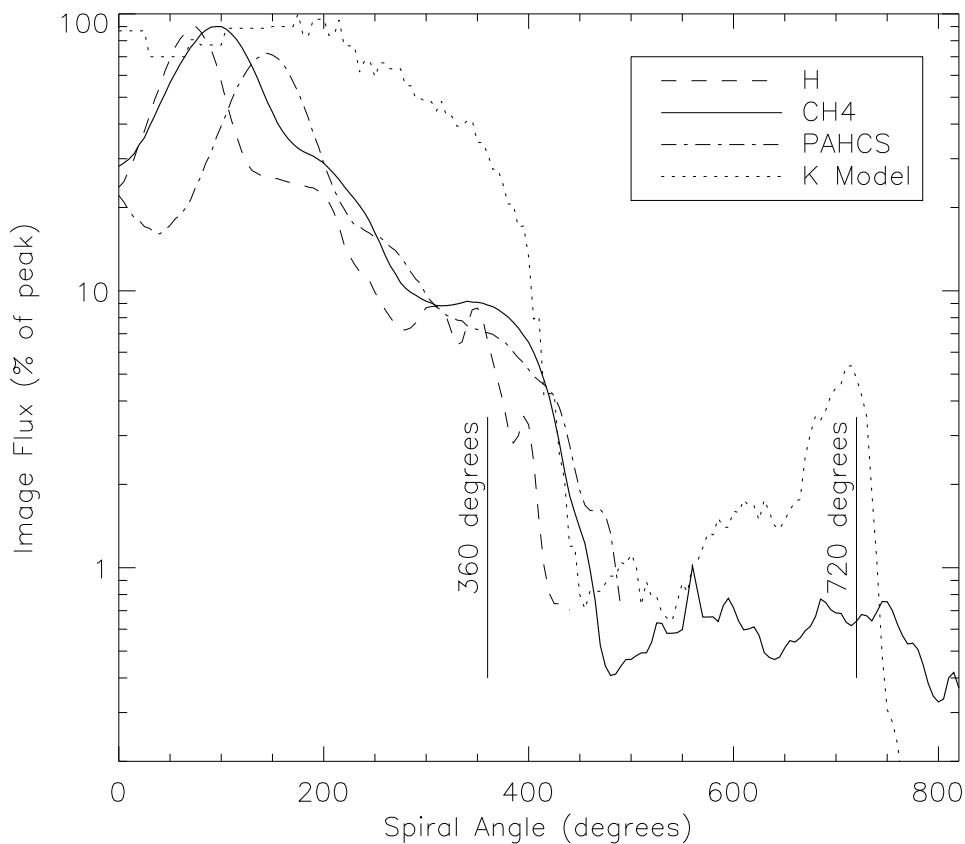


Fig. 6.— Average brightness profile of the plume as a function of angular displacement along the spiral model locus. Data for our three filter bandpasses are given (linetypes indicated in the key) together with a profile extracted from the numerical radiative transfer simulations of Harries et al. (2004) specific to our CH4 filter in the K band. Data for H and PAHCS are terminated shortly after the first full turn, at which point the signal-to-noise in the images is insufficient to discern real structure from noise. For convenience, intervals of 1 and 2 complete revolutions are marked.

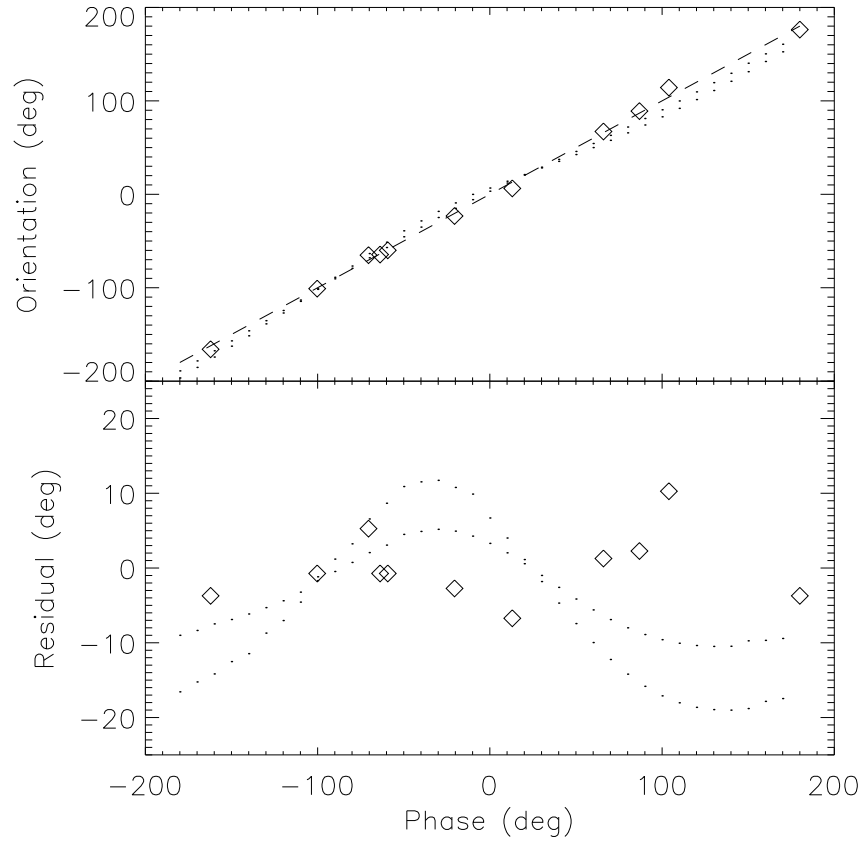


Fig. 7.— (Upper panel) The rotation of the pinwheel at each observing epoch from fits to data in Figure 1, plotted as a function of the orbital phase. The dashed line gives a simple model of uniform angular velocity. (Lower panel) the residual between the data and the uniform model. Both panels have overplotted dotted lines giving examples of expected curves for elliptical orbits with eccentricity $e = 0.1$ and 0.2 .

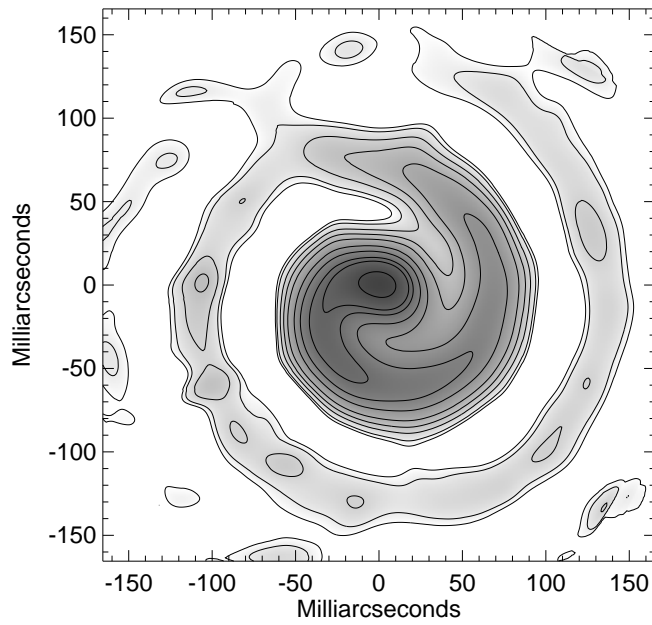


Fig. 8.— Stacked composite image of all epochs of data in the CH4 filter. Contour levels are .1, .2, .5, 1, 2, 5, 10, 20, 30, 70% of the peak. Individual images have been projected to a face-on viewing angle and derotated to the first Apr98 epoch according to the best-fit Archimedian spiral model prior to coadding.

Table 1. Journal of Interferometric Observations.

Date	JD-2450000	Filter
1998 Apr 14	918	H,CH4,PAHCS
1998 Apr 15	919	H,CH4,PAHCS
1998 Jun 04	969	H,CH4,PAHCS
1998 Sep 29	1086	H,CH4,PAHCS
1999 Apr 25	1294	H,CH4,PAHCS
1999 Jul 29	1389	H,CH4,PAHCS
2000 Jun 23	1719	H,CH4,PAHCS
2001 Jun 11	2072	H,CH4
2002 Jul 23	2479	H,CH4
2003 May 12	2772	H,CH4
2004 May 28	3154	H,CH4
2004 Sep 03	3154	H,CH4

Table 2. Properties of Filters

Name	Center (μm)	Bandwidth (μm)
H	1.656	0.333
CH4	2.269	0.155
PAHCS	3.083	0.101